



# Structure-activity relationships of nanoscale $\text{MnO}_x/\text{CeO}_2$ heterostructured catalysts for selective oxidation of amines under eco-friendly conditions

Putla Sudarsanam<sup>a</sup>, Brendan Hillary<sup>a</sup>, Mohamad Hassan Amin<sup>a</sup>,  
Sharifah Bee Abd Hamid<sup>b</sup>, Suresh K. Bhargava<sup>a,\*</sup>

<sup>a</sup> Centre for Advanced Materials and Industrial Chemistry (CAMIC), School of Applied Sciences RMIT University, Melbourne, VIC 3001, Australia

<sup>b</sup> Nanotechnology and Catalysis Research Center (NANOCAT), Institute of Postgraduate Studies (IPS), University of Malaya, 3rd Floor, Block A, 50603 Kuala Lumpur, Malaysia

## ARTICLE INFO

### Article history:

Received 15 September 2015

Received in revised form

10 November 2015

Accepted 12 December 2015

Available online 17 December 2015

### Keywords:

Nanocatalysts

Manganese oxide

Ceria morphology

Characterization

Eco-friendly amine oxidation

## ABSTRACT

The structure-activity properties of  $\text{MnO}_x/\text{CeO}_2$  nanorods and  $\text{MnO}_x/\text{CeO}_2$  nanoparticles, with the importance of  $\text{CeO}_2$  morphology have been investigated for the solvent-free oxidation of amines using oxygen as a green oxidant. The physicochemical properties of the samples have been investigated using HRTEM, XRD, Raman, BET, XPS, and FT-IR techniques. HRTEM studies reveal that  $\text{CeO}_2$  nanorods preferentially expose  $\{110\}$  and  $\{100\}$  crystal planes, while  $\text{CeO}_2$  nanoparticles expose  $\{111\}$  planes. The addition of manganese to  $\text{CeO}_2$  supports leads to an enhancement in the concentration of  $\text{Ce}^{3+}$  ions and oxygen vacancies, which are more pronounced for the  $\text{MnO}_x/\text{CeO}_2$  nanorods as evidenced by Raman and XPS studies. Another striking observation noticed from XPS studies is that  $\text{MnO}_x/\text{CeO}_2$  nanorods catalyst exhibits  $\text{Mn}^{4+}$ ,  $\text{Mn}^{3+}$ , and  $\text{Mn}^{2+}$  species, whereas only  $\text{Mn}^{4+}$  and  $\text{Mn}^{3+}$  are presented in  $\text{MnO}_x/\text{CeO}_2$  nanoparticles catalyst. It was found that  $\text{MnO}_x/\text{CeO}_2$  nanorods catalyst exhibit a two-fold higher activity for the oxidation of benzylamine with superior selectivity to dibenzylimine ( $\sim 99\%$ ) compared with that of  $\text{MnO}_x/\text{CeO}_2$  nanoparticles catalyst. The  $\text{MnO}_x/\text{CeO}_2$  nanorods catalyst was also found to be effective for the oxidation of various amines, and moderate to good product yields were obtained. Novel probable reaction pathways are proposed for solvent-free oxidation of primary and secondary benzylamines over  $\text{MnO}_x/\text{CeO}_2$  nanorods catalyst. The presence of surface-active  $\text{Mn}^{4+}/\text{Mn}^{2+}$  couple and the enhanced defect structure of  $\text{CeO}_2$  nanorods (i.e., higher numbers of  $\text{Ce}^{3+}$  ions and abundant O vacancies) are found to be key factors for the high catalytic efficiency of the  $\text{MnO}_x/\text{CeO}_2$  nanorods.

© 2015 Elsevier B.V. All rights reserved.

## 1. Introduction

Catalysis using nanomaterials, known as ‘nanocatalysis’, is currently the subject of intense investigations because of its increasing importance for potential applications in ‘sustainable chemical industry’ [1–3]. This significance is due to the unique properties of nanocatalysts, such as large surface-to-volume ratio, abundant catalytically active domains, and favorable electronic properties. Several forms of nanocatalysts, such as nano-metal oxides, nano-supported catalysts, magnetic nanocatalysts, core-shell nanocatalysts, and graphene-based nanocatalysts have been developed for many important catalytic applications. Among them,

nano-supported catalysts based on M/support (M = active phase) are promising candidates in selective chemical synthesis. This importance has been attributed to the outstanding performance of nano-supported catalysts coupled with their easy separation and facile recyclability. The efficiency of nano-supported catalysts is dependent upon several factors, including particle size, structure of the active phase, chemical composition, and morphology of the support [4]. Particularly, the morphology of the support has a huge effect on the structure-activity properties of nano-supported catalysts. Different shapes often display different exposed surfaces of the particles with distinct crystallographic facets that may modify the structure-catalytic properties of the active phase species [5–8].

Ceria ( $\text{CeO}_2$ ), an abundant rare earth metal oxide, is one of the most extensively studied oxides in heterogeneous catalysis [9–16]. Especially,  $\text{CeO}_2$  is a key component in auto-exhaust three-way catalytic converters for the purification of harmful pollutants, such

\* Corresponding author.

E-mail address: [suresh.bhargava@rmit.edu.au](mailto:suresh.bhargava@rmit.edu.au) (S.K. Bhargava).

as CO, NO<sub>x</sub>, and unburned hydrocarbons, as well as in selective oxidation catalysis. The ability of ceria to exhibit facile redox properties ( $\text{Ce}^{3+} \leftrightarrow \text{Ce}^{4+}$ ), as well as forming and annihilating oxygen vacancies while maintaining structural integrity, is the key to its widespread application in heterogeneous catalysis. These properties greatly depend on the morphology of ceria and its crystal facets; indeed both morphology and crystal facets are related to each other [9–11,16]. CeO<sub>2</sub> in a fluorite structure possesses three low-index facets: (111), (110), and (100). It has been demonstrated that ceria nanorods preferentially expose both (100) and (110) facets, while ceria nanoparticles are dominated by (111) surfaces [6]. The (100)- and (110)-facet dominated surfaces facilitate the migration of lattice oxygen atoms from the bulk to the surface; however, the process is restricted in the (111)-facet dominated surfaces [6,9]. Consequently, abundant oxygen vacancy defects and more Ce<sup>3+</sup> ions can be found on the (110) and (100) surfaces than those on the (111) surfaces. Therefore, it is possible that when the active phase species are deposited on the surface of CeO<sub>2</sub> nanorods and CeO<sub>2</sub> nanoparticles, quite interesting and unusual catalytic activities can be found because of the morphology-dependent properties of CeO<sub>2</sub> supports, such as oxygen vacancy defects and Ce<sup>3+</sup> ions.

Manganese oxide based catalysts are found to be effective for many catalytic processes, such as water oxidation [17], CO oxidation [18], Hg oxidation [19], formaldehyde oxidation [20], oxidation of benzyl alcohol [21], and combustion of volatile organic compounds [22–25]. This wide application of manganese oxide catalysts is due to their economic and environmental benefits, as well as their excellent structural and catalytic properties [26–29]. For example, manganese oxides are cheap and non-toxic materials [28,29]. They exhibit superior physicochemical and redox properties because of the multiple valences of Mn (II–IV & VII) [26]. It has been reported that highly dispersed manganese oxide nanocrystals exhibit better catalytic efficiency compared with their bulk material counterparts due to the enhanced physicochemical properties at the nanoscale range [30,31]. It is therefore expected that the deposition of nanoscale manganese oxide species on shape controlled CeO<sub>2</sub> nano-supports may lead to unusual properties and exceptional catalytic activities.

The main aim of this work is to investigate the effect of ceria morphology on the physicochemical properties and catalytic performance of MnO<sub>x</sub>/CeO<sub>2</sub> nanocatalysts. For this, we developed CeO<sub>2</sub> nanorods and CeO<sub>2</sub> nanoparticles using hydrothermal and precipitation methods, respectively. 10% Mn was deposited on these CeO<sub>2</sub> supports using a wet-impregnation method. A systematic characterization of the materials has been undertaken using a number of analytical techniques, such as transmission electron microscopy (TEM), high resolution TEM (HRTEM), powder X-ray diffraction (XRD), N<sub>2</sub> adsorption-desorption analysis, X-ray photoelectron spectroscopy (XPS), Raman spectroscopy, and Fourier transform infrared spectroscopy (FT-IR) analysis. The catalytic application of MnO<sub>x</sub>/CeO<sub>2</sub> nanocatalysts was studied for the transformation of amines to imines under ecofriendly reaction conditions. Imines are one of the most frequently used ingredients in the chemical industry [32–36]. Especially, imines are key chemicals for the synthesis of medicines, dyes, fragrances, fungicides, pharmaceuticals, and agricultural products. The synthesis of imines conventionally involves the condensation of amines with carbonyl compounds [32]. This process however requires homogeneous Lewis acid catalysts, dehydrating agents, activated aldehydes, and prolonged reaction time. These drastic conditions make this process practically and environmentally unfavorable. The direct oxidative coupling of amine to imine using heterogeneous catalysts is one of most efficient methodologies to overcome the above disadvantages [33]. However, most of the protocols reported use hazardous stoichiometric oxidants and organic solvents, which is undesirable from the viewpoints of sustainable chemical synthesis [35]. Therefore, in this

study the oxidative coupling of amines to imines has been investigated with O<sub>2</sub> as a green oxidant and without solvent. Significant efforts have been undertaken to investigate structure-activity relationships of nanoscale MnO<sub>x</sub>/CeO<sub>2</sub> heterostructured catalysts for the oxidation of amines.

## 2. Experimental

### 2.1. Catalyst preparation

The CeO<sub>2</sub> nanorods were synthesized using a template-free alkaline hydrothermal method. In a typical procedure, the required quantity of Ce(NO<sub>3</sub>)<sub>3</sub>·6H<sub>2</sub>O (Aldrich, AR grade) was dissolved in deionised water under stirring conditions. An aq. NaOH solution (60 mL, 6 M) was added to the Ce solution and the stirring was continued for 30 min at room temperature. The solution was then transferred into a Teflon bottle and sealed tightly in a stainless-steel autoclave. The hydrothermal treatment was performed at 100 °C for 24 h. After cooling to room temperature, the sample was collected, centrifuged several times with deionised water, and oven-dried at 90 °C for 12 h. The sample was calcined at 500 °C for 4 h in air with a heating ramp of 2 °C/min.

The CeO<sub>2</sub> nanoparticles are synthesized using a precipitation method. Briefly, the required amount of NH<sub>4</sub>Ce(NO<sub>3</sub>)<sub>4</sub>·6H<sub>2</sub>O (Aldrich, AR grade) was dissolved in double distilled water. The precipitant (aq. NH<sub>3</sub> solution, 2.5 v/v%) was added slowly to the above solution over a period of 2 h until the pH of the solution reached to ~8.5. The obtained precipitates were decanted, filtered off, washed with double distilled water, and oven dried at 90 °C for 12 h. The sample was then calcined at 500 °C for 4 h in air with a heating ramp of 2 °C/min. The reason for selecting different methods and different Ce precursors is that CeO<sub>2</sub> nanorods can be only synthesized under hydrothermal conditions using Ce(NO<sub>3</sub>)<sub>3</sub>·6H<sub>2</sub>O precursor, whereas precipitation methods employ a NH<sub>4</sub>Ce(NO<sub>3</sub>)<sub>4</sub>·6H<sub>2</sub>O precursor for the synthesis of CeO<sub>2</sub> nanoparticles [37].

The Mn (10 wt.% of Mn with respect to Ce) was loaded on CeO<sub>2</sub> nanorods and CeO<sub>2</sub> nanoparticles using a wet-impregnation method. In brief, the estimated amount of Mn(NO<sub>3</sub>)<sub>2</sub>·4H<sub>2</sub>O (Aldrich, AR grade) was dissolved in deionised water under stirring conditions. Finely powdered CeO<sub>2</sub> was then added to the Mn solution. The excess water was evaporated on a hot plate at approximately 100 °C with stirring conditions. The obtained sample was oven-dried at 100 °C for 12 h and then, calcined at 500 °C for 4 h in air with a heating ramp of 2 °C/min.

### 2.2. Catalyst characterization

The TEM-HRTEM studies were carried out on a JEOL 2100F equipped with a Gatan Orius SC1000 CCD camera. The accelerating voltage of the electron beam was 80 kV. For analysis, the sample was sonicated in acetone for 5–10 min followed by deposition of few drops on a copper grid. The XRD studies were performed using a Rigaku diffractometer with Cu Kα radiation (1.540 Å) as the source. The data was recorded in the two theta range of 10–80° with a step size of 0.02° and a step time of 2.4 s. The average ceria crystallite size of the samples was estimated using Scherrer equation.

N<sub>2</sub> adsorption-desorption analysis was done using a Micromeritics ASAP 2020 instrument at 77 K. Prior to analysis, the sample was degassed under vacuum for 30 min at ambient temperature followed by fast-mode degassing at 423 K for 12 h. Desorption data was used for estimating BET surface area of the samples. Pore volume and pore size of the samples are estimated using Barrett-Joyner-Halenda (BJH) method applied to the desorption leg of the isotherms. Raman experiments were performed using a PerkinElmer-Raman Station 400 F spectrometer equipped

with a liquid N<sub>2</sub> cooled charge coupled device detector and a confocal microscope. A 350 mW near infrared 785 nm laser was used for the analysis. The wavenumber values reported from the spectra are accurate to within 2 cm<sup>-1</sup>.

The XPS studies were performed using a Thermo K-alpha XPS instrument at a pressure less than 10<sup>-7</sup> torr. The general scan and Ce 3d, Mn 2p, and O 1s core level spectra were recorded using Al K $\alpha$  radiation (1486.6 eV) at a pass energy of 50 eV. The core level binding energies were charge corrected with respect to the carbon (C 1s) peak at 284.6 eV. The FT-IR spectra were recorded on a Nicolet 740 FT-IR spectrometer at ambient conditions with a nominal resolution of 4 cm<sup>-1</sup> and averaging 100 spectra.

### 2.3. Catalytic activity studies

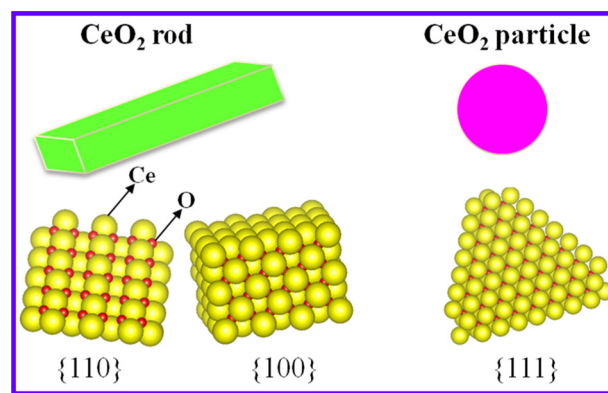
The oxidation of amines was performed using an O<sub>2</sub> balloon under solvent-free conditions. In a typical experiment, 100 mg of catalyst and 3.5 mmol of amine were taken into a 25 mL round bottom flask. The catalyst screening for the oxidation of benzylamine was carried out at 120 °C for 2 h and stirred at 700 rpm. The oxidation of substituted benzylamines, aliphatic amines, and dibenzylamine was conducted using 100 mg of catalyst and 3.5 mmol of amine at the required temperature and time with stirring of 700 rpm. After the reaction, the liquid products and the catalyst were separated by centrifugation. The products and key intermediates presented in Schemes 2 and 3 were confirmed by a Varian CP3800 GC/Saturn 2200MS equipped with a DB-5 capillary column and a thermal conductivity detector. Samples were taken periodically and analyzed using a Shimadzu GC2010 plus equipped with an Rxi-5 ms capillary column and a flame ionization detector. In addition to GC-MS, the key intermediates proposed in Scheme 2 and 3, namely benzaldehyde, benzamide, and benzonitrile are also confirmed by comparing the retention times of authentic chemicals with that of reaction mixture in a Shimadzu GC2010 plus GC. The amine conversion and products selectivity were calculated as per the procedure described elsewhere [35].

## 3. Results and discussions

### 3.1. TEM analysis

The TEM images of CeO<sub>2</sub> supports are shown in Fig. 1. It was obvious that all the supports are in nanoscale range. The CeO<sub>2</sub> nanorods are found to have a uniform diameter of 8 ± 2 nm and a less-uniform length within 30–90 nm. The lattice fringes of CeO<sub>2</sub> nanorods are clearly visible (Fig. 1C and D). The estimated d-spacings were ~0.19 and 0.27 nm, which are assigned to {1 1 0} and {1 0 0} planes of the CeO<sub>2</sub>, respectively (Fig. 1C and D) [38–40]. The angle of 45° with the longitudinal axis indicated the exposure of the {1 0 0} facets and the preferential growth along the [1 1 0] direction [41]. The {1 0 0}- and {1 1 0}-facet dominated surfaces are highly defective and require lower energy for formation of oxygen vacancies, which is beneficial from a catalytic point of view [10]. Conversely, the CeO<sub>2</sub> support synthesized by a precipitation method exhibits different sized particles without any defined morphology (Fig. 1E–H). The average diameter of CeO<sub>2</sub> particles was found to be ~9 ± 3 nm. The estimated d-spacing of fringes in the CeO<sub>2</sub> particles was ~0.31 nm, which corresponds to the spacing of the {1 1 1} phase [6,9]. Scheme 1 shows the representation of CeO<sub>2</sub> nanorods and CeO<sub>2</sub> nanoparticles with preferentially exposed crystal planes.

The TEM images of MnO<sub>x</sub>/CeO<sub>2</sub> nanorods and MnO<sub>x</sub>/CeO<sub>2</sub> nanoparticles are shown in Fig. 2. The manganese oxide nanocrystals on the CeO<sub>2</sub> nano-supports are clearly visible from these images (Fig. S1 of the Supplementary material). The particle size of man-



**Scheme 1.** Representation of CeO<sub>2</sub> nanorods and CeO<sub>2</sub> nanoparticles with preferentially exposed crystal planes.

gane oxide on CeO<sub>2</sub> nanorods and CeO<sub>2</sub> nanoparticles was found to be ~5.2 ± 1 and ~10.4 ± 1 nm, respectively. An interesting observation noticed from TEM images is that different manganese oxide species are found in MnO<sub>x</sub>/CeO<sub>2</sub> nanocatalysts as evidenced by the estimated lattice d-spacings. Mn<sub>3</sub>O<sub>4</sub> and MnO<sub>2</sub> phases were found in MnO<sub>x</sub>/CeO<sub>2</sub> nanorods, whereas MnO<sub>x</sub>/CeO<sub>2</sub> nanoparticles exhibit MnO<sub>2</sub> and Mn<sub>2</sub>O<sub>3</sub> phases (Fig. 2 and Fig. S1 of the Supplementary material).

### 3.2. Powder XRD studies

The X-ray diffraction patterns of CeO<sub>2</sub> supports and MnO<sub>x</sub>/CeO<sub>2</sub> nanocatalysts are presented in Fig. 3. As shown in Fig. 3, all the samples exhibit different reflections at 2 theta values of 28.26, 32.81, 47.29, 56.06, 58.76, 69.23, 76.64, and 78.83° [42,43]. These peaks can be indexed to (1 1 1), (2 0 0), (2 2 0), (3 1 1), (2 2 2), (4 0 0), (3 3 1), and (4 2 0) planes, respectively, indicating the fluorite cubic phase of CeO<sub>2</sub>. A close examination of Fig. 3 reveals that CeO<sub>2</sub> nanorods exhibit the broadest XRD peaks compared with that of CeO<sub>2</sub> nanoparticles. This observation indicates that the CeO<sub>2</sub> nanorods may contain smaller sized crystallites [43]. This is evidenced from the estimated crystallite size of the supports (6.3 and 8.4 nm for CeO<sub>2</sub> nanorods and CeO<sub>2</sub> nanoparticles, respectively) using Scherrer equation (Table 1) [44]. Interestingly, the crystallite size of CeO<sub>2</sub> supports are closer to the particle size of CeO<sub>2</sub> supports obtained from the TEM analysis (~8 ± 2 and 9 ± 3 nm for CeO<sub>2</sub> nanorods and CeO<sub>2</sub> nanoparticles, respectively). Conversely, there was no considerable variation in the crystallite size of the supports after the addition of Mn (Table 1). In addition to the XRD peaks of fluorite CeO<sub>2</sub>, the MnO<sub>x</sub>/CeO<sub>2</sub> nanocatalysts show a few minor reflections at different 2 theta values (Fig. 3). The MnO<sub>x</sub>/CeO<sub>2</sub> nanorods exhibit various XRD peaks at ~36.1 and 59.9°, which indicates the Mn<sub>3</sub>O<sub>4</sub> phase (Fig. 3B) [45–47]. In addition, a Mn<sub>2</sub>O<sub>3</sub> phase (2 theta = 38.76°) was found in MnO<sub>x</sub>/CeO<sub>2</sub> nanorods. In contrast, the MnO<sub>x</sub>/CeO<sub>2</sub> nanoparticles exhibit only a peak at 2 theta of 37.4°, which indicates the presence of a MnO<sub>2</sub> phase (Fig. 3D) [26].

### 3.3. N<sub>2</sub> adsorption-desorption studies

Fig. 4 shows the N<sub>2</sub> adsorption-desorption isotherms of CeO<sub>2</sub> supports and MnO<sub>x</sub>/CeO<sub>2</sub> nanocatalysts. It is interesting to note that the isotherm of MnO<sub>x</sub>/CeO<sub>2</sub> nanoparticles is significantly different compared to that of other samples. Except the MnO<sub>x</sub>/CeO<sub>2</sub> nanoparticles, all the samples show type IV isotherm with H<sub>1</sub>-type hysteresis [16,43,48]. These isotherms are characteristics of mesoporous materials, consisting of well-defined cylindrical-like pore channels. The estimated pore diameters from BJH analysis of CeO<sub>2</sub> nanorods, CeO<sub>2</sub> nanoparticles, and MnO<sub>x</sub>/CeO<sub>2</sub> nanorods clearly



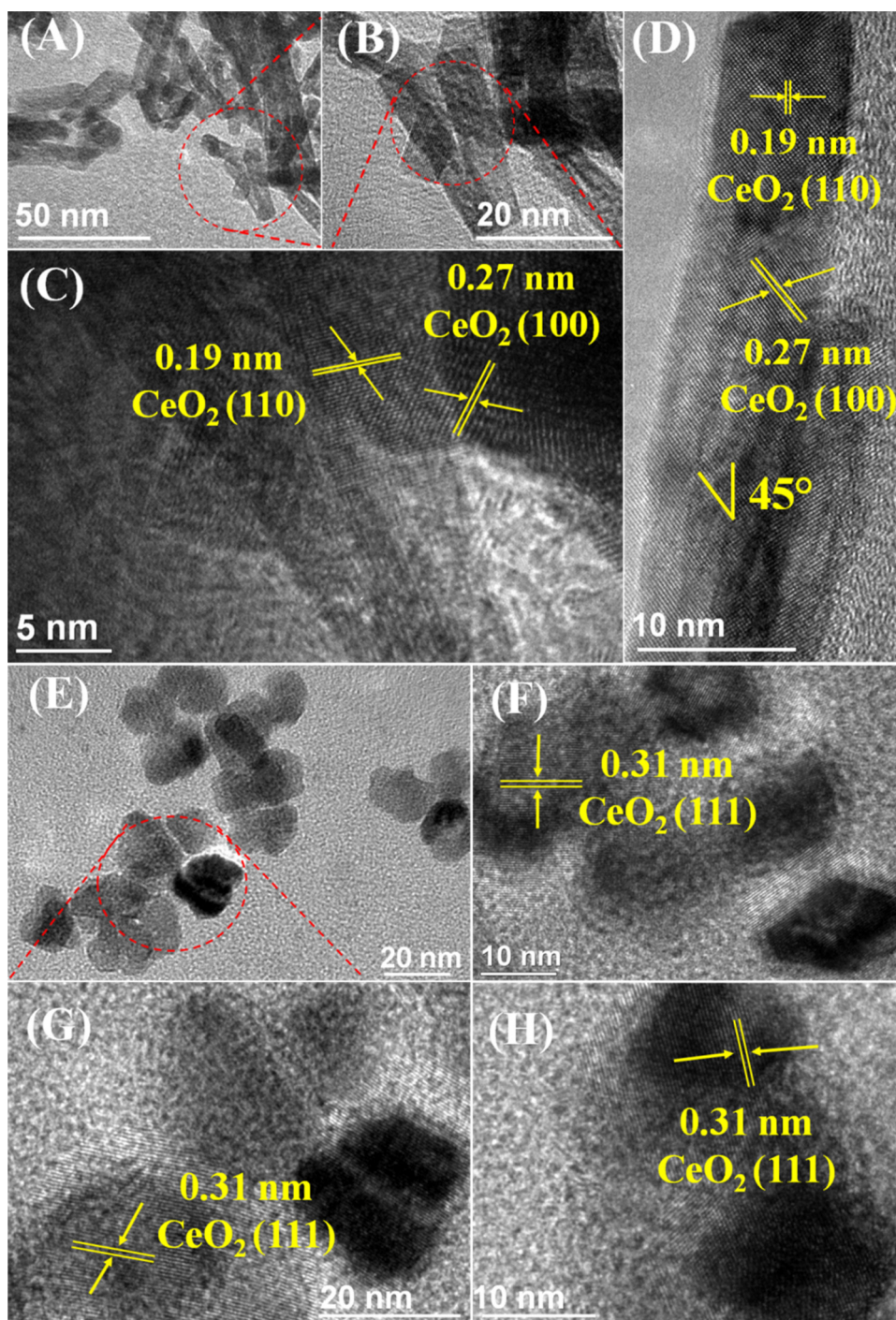


**Fig. 1.** TEM images of CeO<sub>2</sub> nanorods (A–D) and CeO<sub>2</sub> nanoparticles (E–H).

confirm the mesoporous nature of the materials (Table 1). Conversely, the MnO<sub>x</sub>/CeO<sub>2</sub> nanoparticles showed a type IV isotherm with H<sub>2</sub>-type hysteresis, which is due to the interconnectivity of pores. H<sub>2</sub>-type hysteresis loops usually indicate that the distribution of pore size and pore shape is not well defined or irregular [43]. As a result, smaller pore size and pore volume were found for MnO<sub>x</sub>/CeO<sub>2</sub> nanoparticles compared with that of MnO<sub>x</sub>/CeO<sub>2</sub> nanorods (Table 1). The BET surface area of CeO<sub>2</sub> nanoparticles and CeO<sub>2</sub> nanorods were found to be ~39 and 89 m<sup>2</sup> g<sup>−1</sup>, respectively (Table 1). The BET surface area of these supports is considerably improved after the addition of Mn (Table 1). This observation can be explained by two factors: (1) the manganese oxide species are

well-dispersed on the surface of CeO<sub>2</sub> supports and (2) the added Mn increased the thermal stability of CeO<sub>2</sub> supports, which in turn led to a reduction in the aggregation of the particles during the calcination step. The elemental analysis investigated by inductively coupled plasma-mass spectrometer indicates that almost expected compositions of the Mn (~10%) and Ce (~90) were found for all the MnO<sub>x</sub>/CeO<sub>2</sub> catalysts.

### 3.4. Raman studies

Raman spectroscopy is a powerful analytical technique to understand the structural features and lattice defects of CeO<sub>2</sub> and

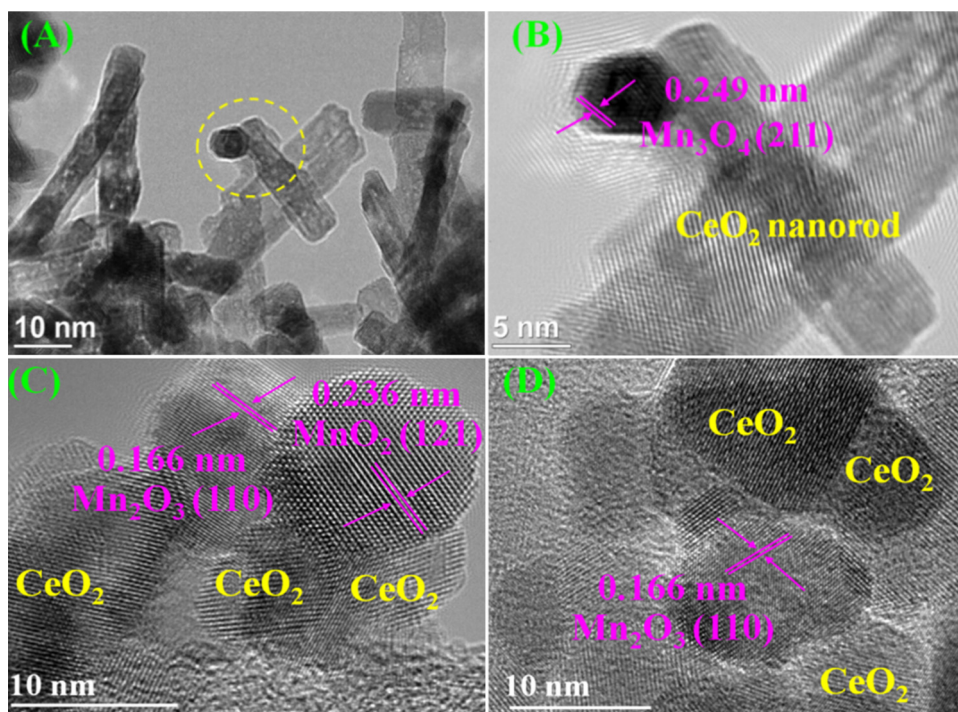


Fig. 2. TEM images of MnO<sub>x</sub>/CeO<sub>2</sub> nanorods (A&B) and MnO<sub>x</sub>/CeO<sub>2</sub> nanoparticles (C&D).

Table 1

Average CeO<sub>2</sub> crystallite size (D), specific surface area (SSA), pore size (P), and pore volume (V) of the CeO<sub>2</sub> supports and MnO<sub>x</sub>/CeO<sub>2</sub> nanocatalysts.

Sample	D (nm) <sup>a</sup>	SSA (m <sup>2</sup> /g) <sup>b</sup>	P (nm) <sup>c</sup>	V (cm <sup>3</sup> /g) <sup>c</sup>
CeO <sub>2</sub> particles	8.4	39	9.818	0.113
MnO <sub>x</sub> /CeO <sub>2</sub> particles	8.6	44	3.575	0.051
CeO <sub>2</sub> rods	6.3	89	12.142	0.396
MnO <sub>x</sub> /CeO <sub>2</sub> rods	6.7	96	10.887	0.316

<sup>a</sup> XRD studies.

<sup>b</sup> N<sub>2</sub> adsorption–desorption analysis.

<sup>c</sup> BJH studies.

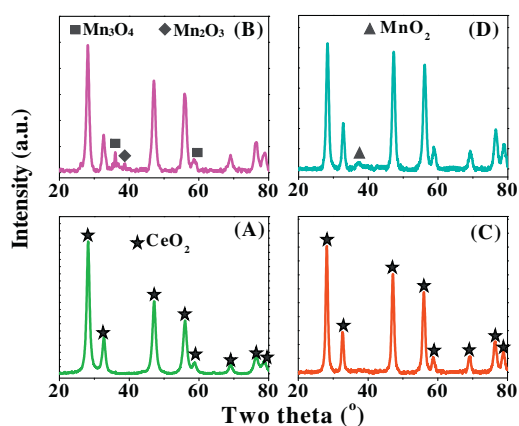


Fig. 3. Powder XRD patterns of CeO<sub>2</sub> nanorods (A), MnO<sub>x</sub>/CeO<sub>2</sub> nanorods (B), CeO<sub>2</sub> nanoparticles (C), and MnO<sub>x</sub>/CeO<sub>2</sub> nanoparticles (D).

MnO<sub>x</sub> based materials [49–53]. Fig. 5 shows Raman spectra of CeO<sub>2</sub> supports and MnO<sub>x</sub>/CeO<sub>2</sub> nanocatalysts. All the samples exhibit a prominent Raman band at ~464 cm<sup>-1</sup>. This band indicates the presence of Raman-active F<sub>2g</sub> mode of fluorite cubic structured CeO<sub>2</sub>, in line with the XRD results (Fig. 3) [49]. The F<sub>2g</sub> band of CeO<sub>2</sub> supports is broadened and shifted to lower wavenumbers after the addition of Mn, which is most pronounced for the MnO<sub>x</sub>/CeO<sub>2</sub> nanorods (Fig.

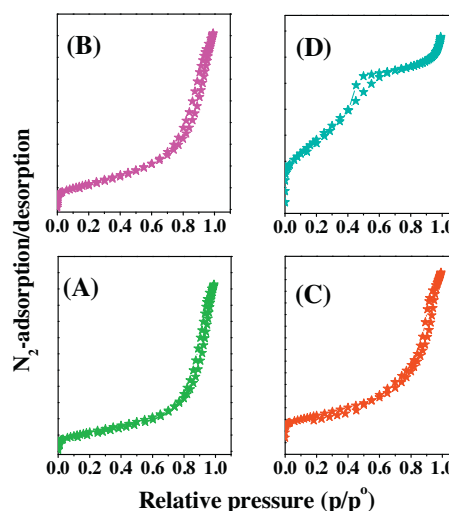


Fig. 4. N<sub>2</sub> adsorption–desorption isotherms of CeO<sub>2</sub> nanorods (A), MnO<sub>x</sub>/CeO<sub>2</sub> nanorods (B), CeO<sub>2</sub> nanoparticles (C), and MnO<sub>x</sub>/CeO<sub>2</sub> nanoparticles (D).

S2 of the Supplementary material). The broad F<sub>2g</sub> band and its shifting indicate the distorted fluorite structured ceria, which may lead to the generation of oxygen vacancies in ceria [12,49]. This is evidenced by the presence of a band at ~580–600 cm<sup>-1</sup> in the Raman



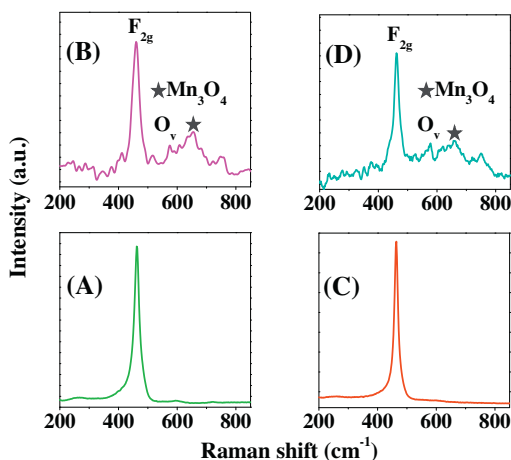


Fig. 5. Raman spectra of CeO<sub>2</sub> nanorods (A), MnO<sub>x</sub>/CeO<sub>2</sub> nanorods (B), CeO<sub>2</sub> nanoparticles (C), and MnO<sub>x</sub>/CeO<sub>2</sub> nanoparticles (D).

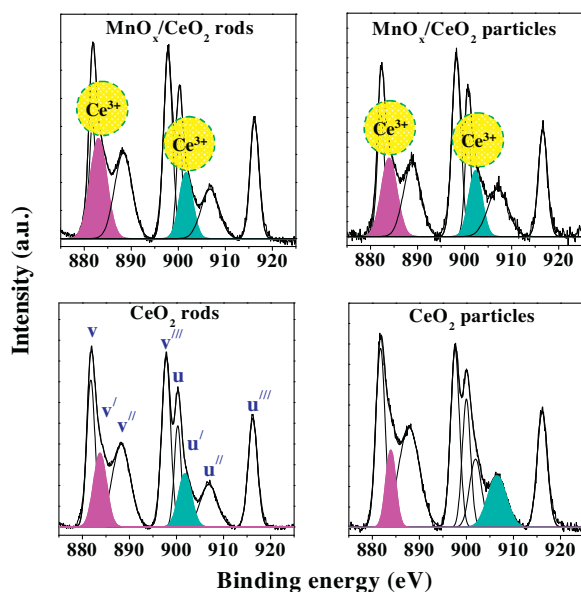


Fig. 6. Ce 3d XPS spectra of CeO<sub>2</sub> nanorods, MnO<sub>x</sub>/CeO<sub>2</sub> nanorods, CeO<sub>2</sub> nanoparticles, and MnO<sub>x</sub>/CeO<sub>2</sub> nanoparticles.

spectra of MnO<sub>x</sub>/CeO<sub>2</sub> nanocatalysts, which is directly related to the oxygen vacancies present in the CeO<sub>2</sub> lattice [49,52]. However, no such band is found in CeO<sub>2</sub> supports. This observation indicates that the addition of Mn to CeO<sub>2</sub> results in the creation of oxygen vacancies, which is attributed to the existence of strong MnO<sub>x</sub>/CeO<sub>2</sub> interactions. It is a well-known fact that the generation of oxygen vacancies is directly related to the conversion of Ce<sup>4+</sup> to Ce<sup>3+</sup>. It is therefore expected that the MnO<sub>x</sub>/CeO<sub>2</sub> samples may contain more Ce<sup>3+</sup> ions compared with that of bare CeO<sub>2</sub> supports, which was investigated with the help of XPS studies (Figs. 6 and 7).

A Raman band was found at about 655 cm<sup>-1</sup> in MnO<sub>x</sub>/CeO<sub>2</sub> nanorods and MnO<sub>x</sub>/CeO<sub>2</sub> nanoparticles, which reveals the presence of Mn<sub>3</sub>O<sub>4</sub> nanoparticles [54]. Interestingly, an apparent Raman band was noticed at ~760 cm<sup>-1</sup> for both MnO<sub>x</sub>/CeO<sub>2</sub> catalysts, which is due to the presence of smaller Mn<sub>3</sub>O<sub>4</sub> grains [55]. The observed IR peaks in the range of 500–680 cm<sup>-1</sup> from the FT-IR analysis provided further evidence of presence of Mn-O and Mn-O-Mn in the synthesized MnO<sub>x</sub>/CeO<sub>2</sub> nanocatalysts (Fig. S3 of the Supplementary material) [56,57].

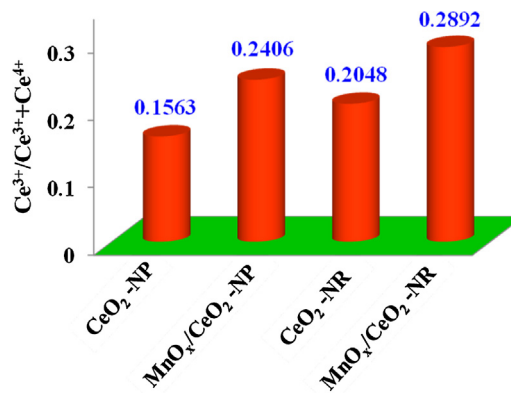


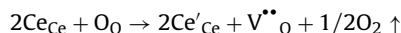
Fig. 7. Concentration of Ce<sup>3+</sup> ions in CeO<sub>2</sub> nanoparticles (CeO<sub>2</sub>-NP), MnO<sub>x</sub>/CeO<sub>2</sub> nanoparticles (MnO<sub>x</sub>/CeO<sub>2</sub>-NP), CeO<sub>2</sub> nanorods (CeO<sub>2</sub>-NR), and MnO<sub>x</sub>/CeO<sub>2</sub> nanorods (MnO<sub>x</sub>/CeO<sub>2</sub>-NR).

### 3.5. XPS studies

XPS analysis was carried out to characterize the valence state of Ce and Mn ions as well as to estimate their strength in the synthesized samples. Fig. 6 shows the Ce 3d XPS spectra of CeO<sub>2</sub> supports and MnO<sub>x</sub>/CeO<sub>2</sub> nanocatalysts. As shown in Fig. 6, the Ce 3d XPS spectra are deconvoluted into 8 well-resolved peaks [58,59]. The symbols of v and u represent the spin-orbit coupling of Ce 3d<sub>5/2</sub> and Ce 3d<sub>3/2</sub>, respectively. In detail, the peaks labeled as v (882.3 eV), v' (888.4 eV), v'' (898.3 eV), u (900.9 eV), u' (907.4 eV), and u'' (916.7 eV) are ascribed to Ce<sup>4+</sup> ions. The peaks denoted as v' (884.7 eV) and u' (903.3 eV) are characteristics of Ce<sup>3+</sup> ions. It was clear that all the samples contain both Ce<sup>3+</sup> and Ce<sup>4+</sup> ions. The concentration of Ce<sup>3+</sup> in the CeO<sub>2</sub> supports and MnO<sub>x</sub>/CeO<sub>2</sub> nanocatalysts was estimated from the ratio of integrated Ce<sup>3+</sup> peaks (u' and v') to the total Ce as follows [16,49]

$$\text{Ce}^{3+} \text{ concentration} = \frac{I(\text{Ce}^{3+})}{I(\text{Ce}^{3+}) + I(\text{Ce}^{4+})}$$

The obtained results are shown in Fig. 7. It was found that CeO<sub>2</sub> nanorods exhibit higher numbers of Ce<sup>3+</sup> ions compared with that of CeO<sub>2</sub> nanoparticles. Interestingly, the addition of Mn to CeO<sub>2</sub> supports leads to an enhancement in the concentration of Ce<sup>3+</sup> ions. This observation indicates that the Mn addition has a favorable effect on the redox properties of CeO<sub>2</sub> supports. Among those, the MnO<sub>x</sub>/CeO<sub>2</sub> nanorods exhibit higher numbers of Ce<sup>3+</sup> ions, indicating the existence of strong interactions between the manganese oxide species and CeO<sub>2</sub> nanorods, in line with the Raman results (Fig. 5). The formation and stabilization of Ce<sup>3+</sup> and oxygen vacancies in CeO<sub>2</sub> lattice of MnO<sub>x</sub>/CeO<sub>2</sub> samples is indicated by Kröger–Vink equation as follows [60]



where Ce<sub>Ce</sub> indicates Ce<sup>4+</sup> in the lattice site of ceria, O<sub>O</sub> is an oxygen atom on an oxygen lattice site of ceria, Ce'<sub>Ce</sub> signifies Ce<sup>3+</sup> in the lattice site of ceria with singular negative charge, and V<sup>••</sup><sub>O</sub> is an oxygen vacancy with double positive charge in ceria lattice.

Fig. 8 shows Mn 2p XPS spectra of MnO<sub>x</sub>/CeO<sub>2</sub> nanocatalysts. The deconvolution of Mn 2p XPS spectra reveals that MnO<sub>x</sub>/CeO<sub>2</sub> particles exhibit two peaks, while the MnO<sub>x</sub>/CeO<sub>2</sub> rods exhibit three peaks. Literature reports reveal that the Mn 2p XPS spectrum of MnO<sub>x</sub>-CeO<sub>2</sub> catalysts shows different binding energies at ~640.3–640.7, 641.6–642.3, and 643.2–644.5 eV corresponding to Mn<sup>2+</sup>, Mn<sup>3+</sup>, and Mn<sup>4+</sup>, respectively [38–62]. It is therefore clear that MnO<sub>x</sub>/CeO<sub>2</sub> particles exhibit only Mn<sup>3+</sup> and Mn<sup>4+</sup> species. Conversely, the MnO<sub>x</sub>/CeO<sub>2</sub> rods show Mn<sup>2+</sup>, Mn<sup>3+</sup> and Mn<sup>4+</sup> species.

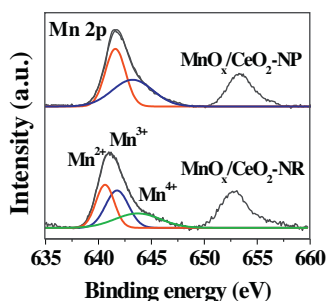


**Fig. 8.** Mn 2p XPS spectra of  $\text{MnO}_x/\text{CeO}_2$  nanorods ( $\text{MnO}_x/\text{CeO}_2\text{-NR}$ ) and  $\text{MnO}_x/\text{CeO}_2$  nanoparticles ( $\text{MnO}_x/\text{CeO}_2\text{-NP}$ ).

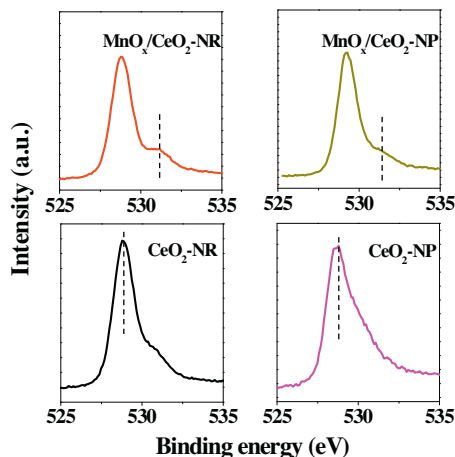


**Fig. 9.** O 1s XPS spectra of  $\text{CeO}_2$  nanorods ( $\text{CeO}_2\text{-NR}$ ),  $\text{MnO}_x/\text{CeO}_2$  nanorods ( $\text{MnO}_x/\text{CeO}_2\text{-NR}$ ),  $\text{CeO}_2$  nanoparticles ( $\text{CeO}_2\text{-NP}$ ), and  $\text{MnO}_x/\text{CeO}_2$  nanoparticles ( $\text{MnO}_x/\text{CeO}_2\text{-NP}$ ).

The presence of  $\text{Mn}^{2+}$  (640.5 eV) and  $\text{Mn}^{3+}$  (641.8 eV) confirm the  $\text{Mn}_3\text{O}_4$  phase in  $\text{MnO}_x/\text{CeO}_2$  rods, in line with the TEM (Fig. 2B) and XRD results (Fig. 3B) [63]. Another interesting observation noticed from Fig. 8 is that the binding energy of  $\text{Mn}^{4+}$  in  $\text{MnO}_x/\text{CeO}_2$  rods is considerably higher compared with that of  $\text{MnO}_x/\text{CeO}_2$  particles. This observation obviously indicates the existence of a strong interaction between the manganese oxide species and  $\text{CeO}_2$  nanorods. Fig. 9 shows O 1s XP spectra of the  $\text{CeO}_2$  supports and  $\text{MnO}_x/\text{CeO}_2$  catalysts. All the samples exhibit two peaks, revealing the presence of two types of oxygen species [16,49,64]. The noticed band at a lower binding energy ( $\sim 529.15$  eV) can be assigned to  $\text{O}_2$  ions in the  $\text{CeO}_2$  and/or manganese oxide lattice. The band at a higher binding energy ( $\sim 531.74$  eV) arises from the adsorbed hydroxyl groups and/or defect oxygen species present on the surface of the catalysts.

### 3.6. Oxidation of benzylamine

The oxidation of benzylamine was selected as a model reaction for screening the catalytic efficiency of  $\text{MnO}_x/\text{CeO}_2$  nanocatalysts. The experiments were performed under conditions that gave low conversion, so that difference in reactivity of the  $\text{MnO}_x/\text{CeO}_2$  catalysts could be readily differentiated [65]. For comparison, the catalytic efficiency of  $\text{CeO}_2$  supports was also investigated under identical conditions. The results are summarized in Table 2. The reaction was initially carried out in the absence of catalyst (entry 1, Table 2), and negligible conversion of benzylamine was found (1.5%). This observation obviously indicates the necessity of a catalyst in the solvent-free oxidation of benzylamine. On the other hand, very low benzylamine conversions were found for the  $\text{CeO}_2$  supports (entries 2–3, Table 2). To our delight, high conversions

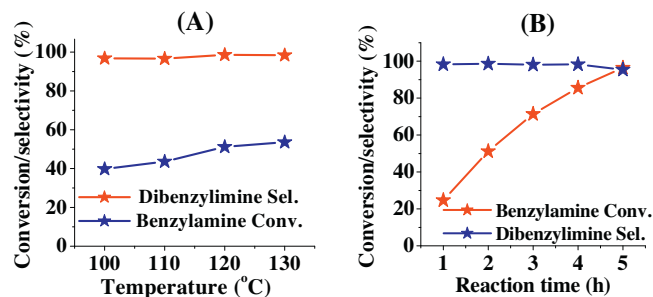


**Fig. 10.** (A) Effect of reaction temperature on the oxidation of benzylamine over  $\text{MnO}_x/\text{CeO}_2$  nanorods catalyst. Reaction conditions: catalyst (100 mg), benzylamine (3.5 mmol),  $\text{O}_2$  balloon, and reaction time (2 h). (B) Effect of reaction time on the oxidation of benzylamine over  $\text{MnO}_x/\text{CeO}_2$  nanorods catalyst. Reaction conditions: catalyst (100 mg), benzylamine (3.5 mmol),  $\text{O}_2$  balloon, and reaction temperature ( $120^\circ\text{C}$ ).

of benzylamine were observed when using the  $\text{MnO}_x/\text{CeO}_2$  catalysts: 29.5 and 51.2% of benzylamine conversions were found for  $\text{MnO}_x/\text{CeO}_2$  particles and  $\text{MnO}_x/\text{CeO}_2$  rods, respectively (entries 4–5, Table 2). This observation evidently indicates the catalytic role of manganese oxide nanocrystals dispersed on the  $\text{CeO}_2$  supports in the solvent-free oxidation of benzylamine with oxygen.

The major product in all of the above reactions was dibenzylimine, with small amounts of benzonitrile and benzamide (Table 2). The selectivity of dibenzylimine was extremely high for the  $\text{CeO}_2$  supports (entries 2–3, Table 2); however this is most likely due to the low conversion of benzylamine, resulting in non-detectable peaks for the minor products. As conversion increased markedly when using the  $\text{MnO}_x/\text{CeO}_2$  nanocatalysts, minor products as a result of secondary reactions were apparent (Scheme 2). Among the  $\text{MnO}_x/\text{CeO}_2$  nanocatalysts, the  $\text{MnO}_x/\text{CeO}_2$  nanorods exhibit a higher benzylamine conversion (51.2%) along with superior imine selectivity (98.6%). The estimated TOF values reveal that the  $\text{MnO}_x/\text{CeO}_2$  rods show the highest catalytic performance in the oxidation of benzylamine (entries 4–5, Table 2). It is interesting to note that the  $\text{MnO}_x/\text{CeO}_2$  nanorods exhibit a very low catalytic performance in the oxidation of benzylamine under a nitrogen atmosphere (entry 6, Table 2). This observation indicates the necessity of the oxygen for efficient conversion of benzylamine to dibenzylimine. As reported earlier, a small amount of benzamide was found when using  $\text{MnO}_x/\text{CeO}_2$  particles and  $\text{MnO}_x/\text{CeO}_2$  rods (Table 2), which could be due to the hydration of benzonitrile (Scheme 2) [66]. This is a very interesting observation because amides are important compounds widely used in the production of pharmaceuticals, agrochemicals, and biomolecules [67]. It would be expected that the presence of excess water enhances the rate of hydration of benzonitrile to yield the benzamide. To understand this, we performed a reaction with an excess amount of water using  $\text{MnO}_x/\text{CeO}_2$  nanorod catalyst, but a very low conversion of benzylamine was found (entry 7, Table 2). To our surprise, no benzamide was found in the aqueous atmosphere, which is most likely due to the low conversion of benzylamine. This observation reveals that excess water has blocked the active sites present in the  $\text{MnO}_x/\text{CeO}_2$  nanorod catalyst, lowering its catalytic efficiency in the benzylamine oxidation reaction.

A significant decrease in the conversion of benzylamine was observed at room temperature when using the  $\text{MnO}_x/\text{CeO}_2$  nanorod catalyst, indicating the necessity of temperature for this reaction (entry 8, Table 2). In order to understand the effect of temperature on benzylamine conversion and product selectivity, the reaction was performed at different temperature intervals in the range of  $100\text{--}130^\circ\text{C}$  using  $\text{MnO}_x/\text{CeO}_2$  nanorod catalyst (Fig. 10A). The conversion of benzylamine was found to be 39.8% at  $100^\circ\text{C}$ . As shown in Fig. 10A, the conversion of benzylamine increases

**Table 2**  
Solvent-free oxidation of benzylamine over CeO<sub>2</sub> supports and MnO<sub>x</sub>/CeO<sub>2</sub> nanocatalysts<sup>a</sup>.

Benzylamine (1a)		Dibenzylimine (2a)		Benzonitrile (2b)		Benzamide (2c)
Entry	Catalyst	Conversion (%) 1a	Selectivity (%) 2a	2b	2c	TOF <sup>e</sup>
1	Blank	1.5	100	–	–	–
2	CeO <sub>2</sub> particles	2.5	100	–	–	–
3	CeO <sub>2</sub> rods	2.7	100	–	–	–
4	MnO <sub>x</sub> /CeO <sub>2</sub> particles	29.5	97.4	1.7	0.9	2.4
5	MnO <sub>x</sub> /CeO <sub>2</sub> rods	51.2	98.6	1.1	0.3	4.9
6 <sup>b</sup>	MnO <sub>x</sub> /CeO <sub>2</sub> rods	3.7	100	–	–	0.4
7 <sup>c</sup>	MnO <sub>x</sub> /CeO <sub>2</sub> rods	4.1	99.4	0.6	–	0.5
8 <sup>d</sup>	MnO <sub>x</sub> /CeO <sub>2</sub> rods	4.7	99.6	0.4	–	0.6

<sup>a</sup> Reaction conditions: Benzylamine (3.5 mmol), catalyst (100 mg), O<sub>2</sub> balloon, time (2 h) and temperature (120 °C).

<sup>b</sup> N<sub>2</sub> balloon.

<sup>c</sup> Water (2 mL).

<sup>d</sup> Room temperature.

<sup>e</sup> TOF = number of moles of amine converted per mole of manganese per hour.

**Table 3**  
Solvent-free oxidation of various amines with molecular oxygen using MnO<sub>x</sub>/CeO<sub>2</sub> nanorod catalyst<sup>a</sup>.

Entry	Substrate	Time (h)	Temperature (°C)	Amine conversion (%)	Product selectivity (%) <sup>b</sup>
1		5	120	98.4	 (95.4)
2 <sup>c</sup>		5	120	64.4	 (84.6)
3 <sup>d</sup>		5	120	77.5	 (93.6)
4		5	120	69.4	 (98.7)
5		7	130	93.5	 (98.9)
6 <sup>e</sup>		7	140	82.4	 (69.5)
7		5	60	10.5	 (99.2)
8		16	60	78.6	 (98.8)
9		5	120	59.4	 (100)
10		24	120	95.6	 (100)

<sup>a</sup> Reaction conditions: Amine (3.5 mmol), catalyst (100 mg), and O<sub>2</sub> balloon.

<sup>b</sup> Other products are nitrile and amide.

<sup>c</sup> Nitrile (14.2%) and amide (1.2%).

<sup>d</sup> Nitrile (5.8%) and amide (0.6%).

<sup>e</sup> Benzaldehyde (17.9%), benzonitrile (6.3%), benzamide (5.5%) and benzylamine (0.8%).

with the increase of temperature. Interestingly, the increase in the conversion of benzylamine was quite low when the temperature increased from 100 to 110 °C (3.8%) compared to from 110 to 120 °C (7.6%). Another striking observation noticed from Fig. 10A is that the selectivity of dibenzylimine was quite low at 100 and 110 °C (96.8 and 96.6%, respectively) than at 120 °C (98.6%). With the

increase of temperature from 120 to 130 °C, however there was no considerable variation in the benzylamine conversion (53.6%) and imine selectivity (98.4%). These interesting observations suggest that 120 °C is the optimum temperature for solvent-free oxidation of benzylamine with oxygen when using MnO<sub>x</sub>/CeO<sub>2</sub> nanorods catalyst. Subsequently, time-dependent experiments were carried



**Table 4**  
Oxidation of dibenzylamine using  $\text{MnO}_x/\text{CeO}_2$  nanorods catalyst with oxygen<sup>a</sup>.

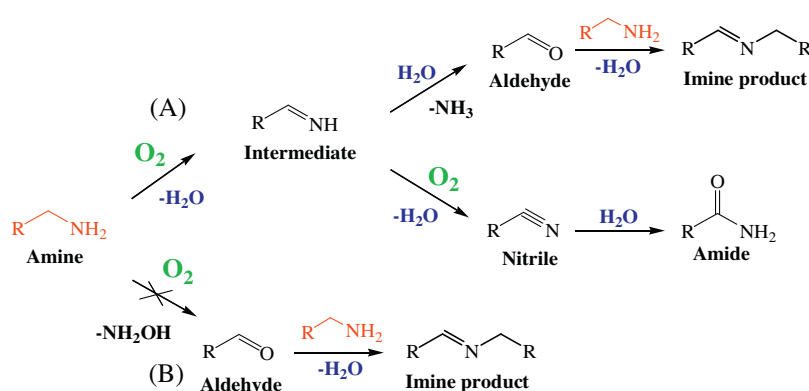
Reaction scheme showing the oxidation of dibenzylamine (1a) to dibenzylimine (2a) and various products (2b, 2c, 2d, 2e) using a catalyst and  $O_2$ .

1a: c1ccccc1CN(Cc2ccccc2)    2a: c1ccccc1C=N(Cc2ccccc2)    2b: Nc1ccccc1    2c: O=Cc1ccccc1    2d: N#Cc1ccccc1    2e: NC(=O)c1ccccc1

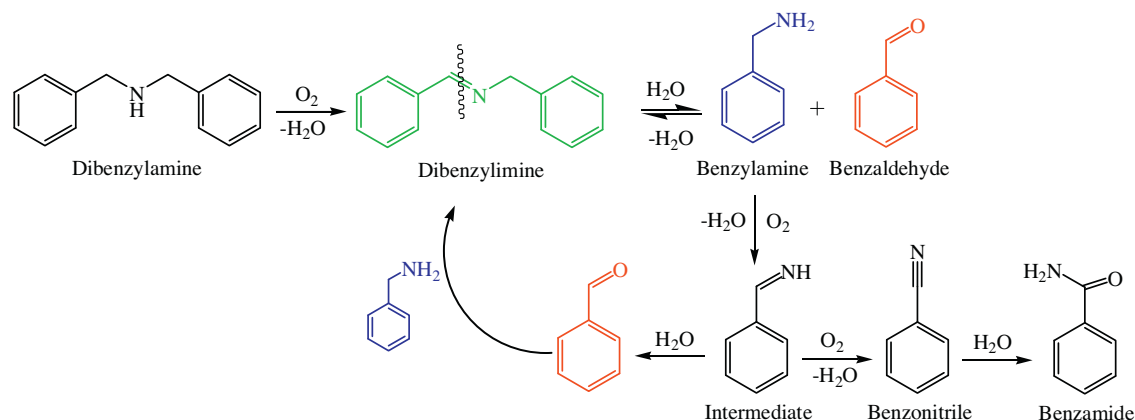
Entry	Substrate	Time (h)	Temperature (°C)	Conversion 1a (%)	Selectivity (%)				
					2a	2b	2c	2d	2e
1	Dibenzylamine	7	140	88.3	69.5	0.6	15.6	5.5	4.8
2	Dibenzylamine	1	120	13.9	91.4	1.5	3.9	2.0	1.2
3	Dibenzylamine	5	120	48.9	87.5	0.6	5.6	2.5	3.8
4 <sup>b</sup>	Dibenzylamine	5	110	9.4	91.9	–	5.2	2.3	0.6

<sup>a</sup> Reaction conditions: dibenzylamine (3.5 mmol), catalyst (100 mg), and  $\text{O}_2$  balloon.

<sup>b</sup> Toluene solvent (5 mL).



**Scheme 2.** Possible reaction pathways ((A) oxidative dehydrogenation of amine and (B) oxygenation of amine) for the oxidation of amines.



**Scheme 3.** Possible reaction pathways in oxidation of dibenzylamine over  $\text{MnO}_x/\text{CeO}_2$  nanorods catalyst with molecular oxygen.

out for the oxidation of benzylamine using  $\text{MnO}_x/\text{CeO}_2$  nanorods catalyst at 120 °C (Fig. 10B). The conversion of benzylamine was considerably increased with reaction time. A 96.4% benzylamine conversion was found at 5 h reaction time. Conversely, there was no considerable change in the selectivity of dibenzylimine (in the range of 98.1–98.6%) with the increase of reaction time up to 4 h. Surprisingly, a considerable decrease in the selectivity of dibenzylimine (~95.4%) was found after 5 h, with small amounts of benzaldehyde (1.1%), benzonitrile (1.7%) and benzamide (1.8%).

### 3.7. Oxidation of various amines using $\text{MnO}_x/\text{CeO}_2$ nanorods catalyst

We have further explored the applicability of  $\text{MnO}_x/\text{CeO}_2$  nanorods catalyst for the oxidation of various amines, including substituted benzylamines, secondary benzylamines, and aliphatic amines. The results are presented in Table 3. The  $\text{MnO}_x/\text{CeO}_2$  nanorods catalyst was effective for the oxidation of substituted benzylamines (entries 2–5, Table 3); however, conversions were low compared with that of pure benzylamine (entry 1, Table 3). Hence, high temperature (130 °C) as well as much longer reaction

time (7 h) was required for achieving good yields in the oxidation of substituted benzylamines (entry 5, Table 3). A higher conversion was found for *p*-substituted benzylamines (entries 3–4, Table 3) compared to that of *o*-substituted benzylamine (entry 2, Table 3). This observation is due to the steric hindrance of substituent at the *o*-position of the phenyl ring of benzylamine. To our surprise, very low selectivity for dibenzylimine was found in the oxidation of *o*-substituted benzylamine (entry 2, Table 3).

Lower amine conversion was found in the oxidation of dibenzylamine (entry 6, Table 3) even higher temperatures and longer reaction times are used. Surprisingly, very low selectivity for dibenzylimine (69.5%) was found, with considerable amounts of benzaldehyde (17.9%), benzonitrile (6.3%), and benzamide (5.5%). A small amount of benzylamine (0.8%) was also found in the oxidation of dibenzylamine. Much longer reaction times were required for the conversion of aliphatic amines (entries 7–10, Table 3). This is due to the lack of active groups attached to  $\text{NH}_2$  of the aliphatic amines. Furthermore, quite interesting results were found toward the selectivity of the products. Almost 99% selectivity for the imine product was found in the butylamine oxidation (entries 7–8, Table 3). Conversely, only a nitrile product was found in the oxidation of octylamine (entries 9–10, Table 3). The hydrolysis of imine intermediate to aldehyde followed by its condensation with another molecule of amine may be unfeasible as shown in Scheme 2, which is due to the long chain of the octylamine, hence higher selectivity toward nitrile product in the oxidation of octylamine.

### 3.8. Reaction pathways for solvent-free oxidation of amines with oxygen

The oxidation of amines follows different reaction pathways as shown in Scheme 2. Usually, the oxidative dehydrogenation pathway is proposed for the oxidation of amines, in which an imine intermediate is formed (pathway A) [32,33,35]. The hydrolysis of this intermediate by in-situ generated water gives an aldehyde, which instantly reacts with available amine to yield the final imine product. It is also possible for the imine intermediate to be further oxidized forming a nitrile, which can be hydrolyzed to give an amide, providing a minor fork in pathway A. Conversely, Lang et al. proposed an oxygenation pathway to directly yield the aldehyde in  $\text{TiO}_2$  photocatalysis (pathway B) [67]. The coupling of this aldehyde with available amine gives the imine product. Note that the formation of nitrile is not possible via pathway B. The observation of nitrile and amide products in the present study revealed that the solvent-free oxidation of amines over  $\text{MnO}_x/\text{CeO}_2$  nanocatalysts follows the oxidative dehydrogenation pathway as shown in Scheme 2 (pathway A).

However, some interesting observations were found in the case of oxidation of a secondary benzylamine (entry 6, Table 3). If the reaction proceeds via an oxidative dehydrogenation pathway, 100% selectivity toward dibenzylimine product should be found because only one step is required to yield the dibenzylimine product from the dibenzylamine oxidation reaction (Fig. S4 of the Supplementary material). Surprisingly, significant amounts of other products, such as benzaldehyde, benzonitrile, and benzamide, with a small amount of benzylamine were found in the oxidation of dibenzylamine (entry 6, Table 3). This is only possible if the formed dibenzylimine undergoes hydrolysis, giving benzylamine and benzaldehyde (Scheme 3). These two products can react with each other to reform dibenzylimine as shown in Scheme 3. On the other hand, there are several different ways in which benzylamine can be oxidized resulting in different reactions and products (Scheme 2, pathway A). In order to better understand this, we performed several oxidation experiments using dibenzylamine at different conditions with the  $\text{MnO}_x/\text{CeO}_2$  nanorod catalyst and the results are shown in Table 4. Selectivity toward the dibenzylimine prod-

uct was significantly improved when temperature and/or time were decreased; however, lower temperatures resulted in a lower conversion of dibenzylamine (entries 2–3, Table 4). Considerable amounts of benzaldehyde, benzonitrile, benzamide, and benzylamine even can be found for 1 h at  $120^\circ\text{C}$  (entry 2, Table 4). Biswas et al. reported 99% selectivity toward the dibenzylimine product in the oxidation of dibenzylamine using a  $\text{Cs}/\text{MnO}_x$  catalyst at  $110^\circ\text{C}$  in toluene solvent [32]. For this reason, we also studied the oxidation of dibenzylamine with toluene at  $110^\circ\text{C}$  (entry 4, Table 4). A 91.9% selectivity for dibenzylimine, with 5.2 and 2.3% selectivity of benzaldehyde and benzonitrile, respectively, were found when using toluene as a solvent with  $\text{MnO}_x/\text{CeO}_2$  nanorods catalyst (entry 4, Table 4). Based on the above results, we confirm in-situ hydrolysis of the imine product in the dibenzylamine oxidation reaction. The reason for this strange observation is that in-situ formed water in this reaction has only one pathway - to hydrolyze the imine, cleaving it into benzaldehyde and benzylamine. The benzylamine produced from hydrolysis of imine can be oxidized itself into mainly imine with smaller quantities of nitrile/amide, leaving the benzaldehyde from hydrolysis to slowly build in the reaction vessel as time passes. This is reflected in the experiments conducted and is seen as an increase in the selectivity to benzaldehyde as conversion of dibenzylamine increases (Table 4), which is due to the versatile catalytic properties of  $\text{MnO}_x/\text{CeO}_2$  nanorods.

### 3.9. Structure-activity relationships of $\text{MnO}_x/\text{CeO}_2$ nanocatalysts

A number of factors have been examined including the preparation method, composition, structure, and valence state of manganese to elucidate the key factors accountable for the catalytic performance of the manganese oxide based catalysts [22–24,32]. Among these factors, the valence state of Mn (+2, +3 or +4) is found to play a significant role in the oxidation efficiency of manganese oxide catalysts. For example, Kim et al. found that  $\text{Mn}_3\text{O}_4$  composed of both  $\text{Mn}^{3+}$  and  $\text{Mn}^{2+}$  shows a higher catalytic performance for the oxidation of toluene compared to that of  $\text{Mn}_2\text{O}_3$  and  $\text{MnO}_2$  [23]. Conversely, Peluso et al. suggested that high concentration of  $\text{Mn}^{3+}$  leads to weak MnO bonds, resulting in excellent catalytic performance of manganese oxide catalysts for the oxidation of ethanol [24]. Tang et al. revealed that the presence of  $\text{Mn}^{4+}$  and  $\text{Mn}^{2+}$  species leads to an improvement in the concentration of adsorbed oxygen species and oxygen vacancy defects, respectively, hence superior catalytic performance of manganese oxide for the combustion of volatile organic compounds [22]. Biswas et al. reported that surface-active  $\text{Mn}^{3+}$  species along with labile lattice oxygen play a favorable role in the catalytic activity of  $\text{MnO}_x$ -based catalyst for the oxidation of amines [32]. It can be therefore understood from the literature reports that the distribution of  $\text{Mn}^{2+}$ ,  $\text{Mn}^{3+}$ , and  $\text{Mn}^{4+}$  species show a crucial effect on the catalytic efficiency of manganese oxide; however this is highly dependent on the reactions undertaken and the reaction conditions employed.

The investigated XRD, TEM, Raman, and XPS studies reveal the existence of different manganese oxide phases, depending on the morphology of  $\text{CeO}_2$  supports. Among those studies, XPS results clearly confirmed that  $\text{MnO}_x/\text{CeO}_2$  nanoparticles exhibit only  $\text{Mn}^{3+}$  and  $\text{Mn}^{4+}$  ions, whereas the  $\text{MnO}_x/\text{CeO}_2$  nanorods show  $\text{Mn}^{2+}$ ,  $\text{Mn}^{3+}$ , and  $\text{Mn}^{4+}$  ions (Fig. 8). The presence of  $\text{Mn}^{2+}$  ions leads to generation of oxygen vacancies to maintain the charge neutrality in the manganese oxide lattice [22]. Another striking observation noticed from XPS studies is that  $\text{MnO}_x/\text{CeO}_2$  nanorods exhibit large amounts of  $\text{Ce}^{3+}$  ions, thus abundant oxygen vacancies compared with that of  $\text{MnO}_x/\text{CeO}_2$  nanoparticles (Figs. 6 and 7). The  $\text{Ce}^{3+}$  ions and oxygen vacancies could enhance the mobility of oxygen in the  $\text{MnO}_x/\text{CeO}_2$  nanorods [68,69]. Catalytic activity studies revealed that the  $\text{MnO}_x/\text{CeO}_2$  nanorods exhibit higher catalytic per-

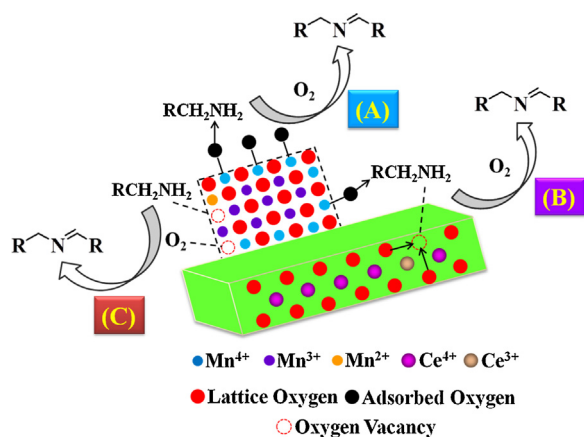


**Fig. 11.** Possible reaction pathways for the solvent-free oxidation of amines over  $\text{MnO}_x/\text{CeO}_2$  nanorods catalyst.

formance in the solvent-free oxidation of amines compared with that of  $\text{MnO}_x/\text{CeO}_2$  nanoparticles (Table 2).

Based on the above results and discussions, possible mechanisms were proposed for the oxidation of amines over  $\text{MnO}_x/\text{CeO}_2$  nanorods catalyst (Fig. 11). A strong relationship between the distribution of surface Mn ions and defect structure of  $\text{CeO}_2$  nanorods can be found in Fig. 11. As shown in Fig. 11,  $\text{Mn}^{4+}$  ions present in the  $\text{MnO}_x/\text{CeO}_2$  nanorods catalyst provide the active oxygen for the oxidation of amine (path A). In path B,  $\text{Ce}^{3+}$  ions and oxygen vacancies present in  $\text{CeO}_2$  nanorods could play a key role in the adsorption and oxidation of amine to imine. Conversely, oxygen vacancies present in the manganese oxide due to the presence of  $\text{Mn}^{2+}$  could activate both gas phase oxygen and amine to yield the imine product (path C). Path A is common for all the  $\text{MnO}_x/\text{CeO}_2$  catalysts because  $\text{Mn}^{4+}$  is presented in all the catalysts (Fig. 8). Path B is more favorable for  $\text{MnO}_x/\text{CeO}_2$  nanorods catalyst because it has large amounts of  $\text{Ce}^{3+}$  and O vacancies compared with that of  $\text{MnO}_x/\text{CeO}_2$  nanoparticles catalyst (Figs. 6 and 7). Conversely, path C is only possible in  $\text{MnO}_x/\text{CeO}_2$  nanorods catalyst as  $\text{Mn}^{2+}$  ions are presented in this catalyst (Fig. 8). Therefore, the distribution of surface  $\text{Mn}^{4+}$  and  $\text{Mn}^{2+}$  ions and the improved defect structure of  $\text{CeO}_2$  nanorods are the key reasons for the high catalytic performance of  $\text{MnO}_x/\text{CeO}_2$  nanorods compared with that of  $\text{MnO}_x/\text{CeO}_2$  nanoparticles for the solvent-free oxidation of amines with molecular oxygen.

### 3.10. Reusability study and characterization of spent $\text{MnO}_x/\text{CeO}_2$ nanorods catalyst

We have further studied the reusability of  $\text{MnO}_x/\text{CeO}_2$  nanorods up to 3 cycles for the oxidation of benzylamine. The catalytic experiments were conducted at the following conditions: 3.5 mmol benzylamine, 120 °C reaction temperature, 5 h reaction time, 100 mg catalyst,  $\text{O}_2$  balloon, and 700 rpm stirring speed. After each experiment, the catalyst was separated from the reaction mixture by centrifugation. The recovered catalyst was then washed with methanol several times and dried at 393 K for 12 h. It was found that the conversion of benzylamine decreases with the repeated use of catalyst: 96.4, 89.6, and 82.3% conversions of benzylamine were found for 1st, 2nd and 3rd cycles, respectively. On the other hand, there was no significant variation in the selectivity of imine product with the repeated use of the catalyst (~95.4–97.6%).

We have conducted TEM and XPS studies of spent  $\text{MnO}_x/\text{CeO}_2$  nanorods to understand key reasons for its deactivation during the oxidation of benzylamine. The obtained TEM images indicate that the particle size and morphology of  $\text{MnO}_x/\text{CeO}_2$  nanorods were not changed significantly after the benzylamine oxidation reaction

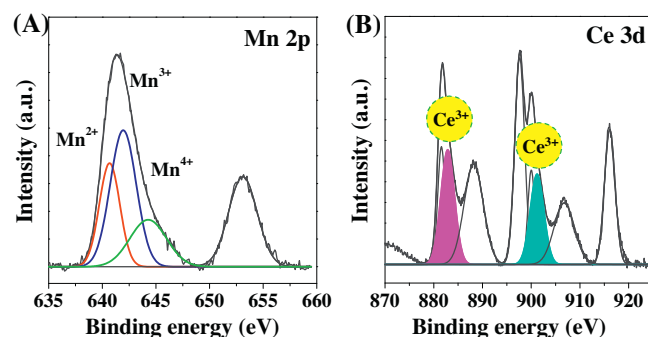


**Fig. 12.** (A) Mn 2p XPS spectrum and (B) Ce 3d XPS spectrum of spent  $\text{MnO}_x/\text{CeO}_2$  nanorods catalyst.

(Fig. S5 of the Supplementary material). The presence of nanosized  $\text{CeO}_2$  rods with an average diameter of  $\sim 8.6 \pm 2$  nm can be noticed from the TEM images of spent catalyst. As well, the estimated lattice d-spacings in the TEM images of  $\text{MnO}_x/\text{CeO}_2$  nanorods reveal the presence of  $\text{Mn}_3\text{O}_4$  and  $\text{MnO}_2$  with an average diameter of  $\sim 7.4 \pm 1.5$  nm.

Since heterogeneous catalytic reactions take place on the catalyst surface, quite interesting observations are noticed from the XPS analysis of spent  $\text{MnO}_x/\text{CeO}_2$  nanorods. Fig. 12A shows the Mn 2p spectrum of spent  $\text{MnO}_x/\text{CeO}_2$  nanorods. As observed in the fresh catalyst (Fig. 8), three Mn species, such as  $\text{Mn}^{2+}$ ,  $\text{Mn}^{3+}$ , and  $\text{Mn}^{4+}$  were also found in the spent  $\text{MnO}_x/\text{CeO}_2$  nanorods. Interestingly, the intensity of  $\text{Mn}^{3+}$  peak is significantly increased with respect to  $\text{Mn}^{4+}$  peak in the spent catalyst compared with that of fresh catalyst (Fig. 8). This observation reveals that some proportion of  $\text{Mn}^{4+}$  species are converted to  $\text{Mn}^{3+}$  during the benzylamine oxidation. This is because  $\text{Mn}^{4+}$  ions provide the active oxygen for the oxidation of amine (Fig. 11), hence conversion of  $\text{Mn}^{4+}$  to  $\text{Mn}^{3+}$  (Fig. 12A). As noticed in the O 1s spectrum of the fresh catalyst (Fig. 9), two peaks were also found in the O 1s spectrum of the spent catalyst, indicating the presence of two oxygen species (Fig. S6 of the Supplementary material). The lower binding energy peak can be ascribed to  $\text{O}_2$  ions in the ceria and/or manganese oxide lattice, while the higher energy peak indicates the presence of adsorbed hydroxyl groups and/or oxygen defect species on the catalyst surface. The Ce 3d spectrum of spent  $\text{MnO}_x/\text{CeO}_2$  nanorods is shown in Fig. 12B. The comparison of Fig. 12B with Fig. 6 (Ce 3d XPS spectra) clearly reveals the presence of both  $\text{Ce}^{3+}$  and  $\text{Ce}^{4+}$  ions in the spent catalyst. A lower concentration of  $\text{Ce}^{3+}$  ions was found for the spent  $\text{MnO}_x/\text{CeO}_2$  nanorods ( $\sim 0.2615$ ) compared with that of the fresh catalyst ( $\sim 0.2892$ , Fig. 7).  $\text{CeO}_2$  is a well-known material for its superior oxygen storage and release ability depending upon the reaction atmospheres. It is therefore possible that  $\text{CeO}_2$  can absorb gas phase oxygen during the benzylamine oxidation, transforming  $\text{Ce}^{3+}$  to  $\text{Ce}^{4+}$ . As shown in Fig. 11,  $\text{Mn}^{4+}$  and  $\text{Ce}^{3+}$  species play a prominent role in the catalytic efficiency of  $\text{MnO}_x/\text{CeO}_2$  nanorods catalyst during the oxidation of benzylamine. Therefore, the decrease in the concentration of  $\text{Mn}^{4+}$  and  $\text{Ce}^{3+}$  species could be the reason for decrease in the catalytic efficiency of  $\text{MnO}_x/\text{CeO}_2$  nanorods for the benzylamine oxidation.

## 4. Conclusions

In summary, the catalytic performance of  $\text{MnO}_x/\text{CeO}_2$  nanocatalysts, prepared with two different morphologies of  $\text{CeO}_2$ , such as nanorods and nanoparticles, was investigated for the solvent-free oxidation of various amines with molecular oxygen. XRD, HRTEM, Raman, and XPS studies reveal the presence of different manganese oxide phases in the synthesized materials led by morphology-tuned  $\text{MnO}_x/\text{CeO}_2$  interactions. Especially,  $\text{MnO}_x/\text{CeO}_2$  nanoparticles dis-



play  $\text{Mn}^{3+}$  and  $\text{Mn}^{4+}$  ions, whereas  $\text{MnO}_x/\text{CeO}_2$  nanorods show  $\text{Mn}^{2+}$ ,  $\text{Mn}^{3+}$ , and  $\text{Mn}^{4+}$  as evidenced by XPS results. Among them,  $\text{MnO}_x/\text{CeO}_2$  nanorods exhibited superior catalytically favorable properties, such as abundant O vacancies and more  $\text{Ce}^{3+}$  sites. It was found that  $\text{MnO}_x/\text{CeO}_2$  nanorods exhibit a two-fold higher activity for the oxidation of benzylamine with almost 99% selectivity to dibenzylimine compared with that of  $\text{MnO}_x/\text{CeO}_2$  nanoparticles. The  $\text{MnO}_x/\text{CeO}_2$  nanorods also exhibited excellent catalytic performance in the oxidation of various substituted benzylamines and aliphatic amines. Surprisingly, in-situ hydrolysis of dibenzylimine to benzaldehyde and benzylamine, and subsequent oxidation of benzylamine was found in the dibenzylamine oxidation reaction with  $\text{MnO}_x/\text{CeO}_2$  nanorod catalyst. The existence of surface-active  $\text{Mn}^{4+}/\text{Mn}^{2+}$  couples and the enhanced defect structure of  $\text{CeO}_2$  are found to be key factors for the high catalytic efficiency of  $\text{MnO}_x/\text{CeO}_2$  nanorods. The excellent performance of  $\text{MnO}_x/\text{CeO}_2$  nanorods catalyst together with the advantages of eco-friendly reaction conditions and economic benefits of the respective oxides could make it potential alternative to noble metal-based catalysts for selective oxidation catalysis.

## Acknowledgments

We thank Dr. Matthew Field, RMIT University for his immense help for technical assistance for characterization. The authors duly acknowledge the RMIT Microscopy and Microanalysis Facility (RMMF) for providing access to their instruments used in this study.

## Appendix A. Supplementary data

Supplementary data associated with this article can be found, in the online version, at <http://dx.doi.org/10.1016/j.apcatb.2015.12.026>.

## References

- [1] M.A. Mahmoud, C.E. Tabor, M.A. El-Sayed, Y. Ding, Z.L. Wang, J. Am. Chem. Soc. 130 (2008) 4590–4591.
- [2] N. Dimitratos, J.A. Lopez-Sanchez, G.J. Hutchings, Chem. Sci. 3 (2012) 20–44.
- [3] Y. Li, W. Shen, Chem. Soc. Rev. 43 (2014) 1543–1574.
- [4] J. Feng, Y. He, Y. Liu, Y. Du, D. Li, Chem. Soc. Rev. 44 (2015) 5291–5319.
- [5] J. Qu, X. Zhou, F. Xu, X.-Q. Gong, S.C.E. Tsang, J. Phys. Chem. C 118 (2014) 24452–24466.
- [6] D. Zhang, X. Du, L. Shi, R. Gao, Dalton Trans. 41 (2012) 14455–14475.
- [7] B.R. Cuenya, J.R. Croy, S. Mostafa, F. Behafarid, L. Li, Z. Zhang, J.C. Yang, Q. Wang, A.I. Frenkel, J. Am. Chem. Soc. 132 (2010) 8747–8756.
- [8] H. Li, G. Qi, X. Tana, Zhang, W. Li, W. Shen, Catal. Sci. Technol. 1 (2011) 1677–1682.
- [9] C. Sun, H. Li, L. Chen, Energy Environ. Sci. 5 (2012) 8475–8505.
- [10] E. Aneggi, D. Wiater, C. de Leitenburg, J. Llorca, A. Trovarelli, ACS Catal. 4 (2014) 172–181.
- [11] A.K.P. Mann, Z. Wu, F.C. Calaza, S.H. Overbury, ACS Catal. 4 (2014) 2437–2448.
- [12] L. Katta, P. Sudarsanam, G. Thirumurthulu, B.M. Reddy, Appl. Catal. B: Environ. 101 (2010) 101–108.
- [13] B.M. Reddy, G. Thirumurthulu, L. Katta, Y. Yamada, S.-E. Park, J. Phys. Chem. C 113 (2009) 15882–15890.
- [14] E.N. Ntainjua, M. Piccinini, J.C. Pritchard, J.K. Edwards, A.F. Carley, C.J. Kiely, G.J. Hutchings, Catal. Today 178 (2011) 47–50.
- [15] P.J. Miedziak, Z. Tang, T.E. Davies, D.I. Enache, J.K. Bartley, A.F. Carley, A.A. Herzing, C.J. Kiely, S.H. Taylo, G.J. Hutchings, J. Mater. Chem. 19 (2009) 8619–8627.
- [16] P. Sudarsanam, B. Hillary, D.K. Deepa, M. Hassan Amin, B. Mallesham, B.M. Reddy, S.K. Bhargava, Catal. Sci. Technol. 5 (2015) 3496–3500.
- [17] C.-H. Kuo, I.M. Mosa, A.S. Poyraz, S. Biswas, A.M. El-Sawy, W. Song, Z. Luo, S.-Y. Chen, J.F. Rusling, J. He, S.L. Suib, ACS Catal. 5 (2015) 1693–1699.
- [18] P. Venkataswamy, K.N. Rao, D. Jampaiah, B.M. Reddy, Appl. Catal. B: Environ. 162 (2015) 122–132.
- [19] H. Li, C.-Y. Wu, Y. Li, J. Zhang, Appl. Catal. B: Environ. 111–112 (2012) 381–388.
- [20] J. Quiroz, J.-M. Giraudon, A. Gervasini, C. Dujardin, C. Lancelot, M. Trentesaux, J.-F. Lamoniér, ACS Catal. 5 (2015) 2260–2269.
- [21] F. Arena, B. Gumina, A.F. Lombardo, C. Espro, A. Patti, L. Spadaro, L. Spiccia, Appl. Catal. B: Environ. 162 (2015) 260–267.
- [22] W. Tang, X. Wu, D. Li, Z. Wang, G. Liu, H. Liu, Y. Chen, J. Mater. Chem. A 2 (2014) 2544–2554.
- [23] S.C. Kim, W.G. Shim, Appl. Catal. B: Environ. 98 (2010) 180–185.
- [24] M.A. Peluso, L.A. Gambaro, E. Pronato, D. Gazzoli, H.J. Thomas, J.E. Sambeth, Catal. Today 133 (2008) 487–492.
- [25] B. Bai, J. Li, J. Hao, Appl. Catal. B: Environ. 164 (2015) 241–250.
- [26] J. Li, L. Li, W. Cheng, F. Wu, X. Lu, Z. Li, Chem. Eng. J. 244 (2014) 59–67.
- [27] Y. Wang, H. Sun, H.M. Ang, M.O. Tade, S. Wang, ACS Appl. Mater. Interfaces 6 (2014) 19914–19923.
- [28] M. Fekete, R.K. Hocking, S.L.Y. Chang, C. Italiano, A.F. Patti, F. Arena, L. Spiccia, Energy Environ. Sci. 6 (2013) 2222–2232.
- [29] Y. Luo, Y.-Q. Deng, W. Mao, X.-J. Yang, K. Zhu, J. Xu, Y.-F. Han, J. Phys. Chem. C 116 (2012) 20975–20981.
- [30] C. Zhiwen, J. Zheng, P. Dengyu, L. Zhen, W. Minghong, S. Chan-Hung, W.C.M. Lawrence, K.L.L. Joseph, Chem. Rev. 112 (2012) 3833–3855.
- [31] H. Enaga, N. Maeda, Y. Nagai, Catal. Sci. Technol. 5 (2015) 3147–3158.
- [32] S. Biswas, B. Dutta, K. Mullick, C.-H. Kuo, A.S. Poyraz, S.L. Suib, ACS Catal. 5 (2015) 439–4403.
- [33] M.T. Schümperli, C. Hammond, I. Hermans, ACS Catal. 2 (2012) 1108–1117.
- [34] R.J. Angelici, Catal. Sci. Technol. 3 (2013) 279–296.
- [35] P. Sudarsanam, A. Rangaswamy, B.M. Reddy, RSC Adv. 4 (2014) 46378–46382.
- [36] C.M. Oprea, O.D. Pavel, A. Moragues, J. El Haskourib, D. Beltrán, P. Amorós, M.D. Marcos, L.E. Stoflea, V. I. Parvulescu, Catal. Sci. Technol. 4 (2014) 4340–4355.
- [37] Y. Li, W. Shen, Chem. Soc. Rev. 43 (2014) 1543–1574.
- [38] R. Gao, D. Zhang, P. Maitarad, L. Shi, T. Rungrotmongkol, H. Li, J. Zhang, W. Cao, J. Phys. Chem. C 117 (2013) 10502–10511.
- [39] P. Zhao, C. Wang, F. He, S. Liu, RSC Adv. 4 (2014) 45665–45672.
- [40] D. Jiang, W. Wang, L. Zhang, Y. Zheng, Z. Wang, ACS Catal. 5 (2015) 4851–4858.
- [41] A. Chen, Y. Zhou, N. Ta, Y. Li, W. Shen, Catal. Sci. Technol. 5 (2015) 4184–4192.
- [42] P. Sudarsanam, K. Kuntaiah, B.M. Reddy, New J. Chem. 38 (2014) 5991–6001.
- [43] P. Sudarsanam, P.R. Selvakannan, S.K. Soni, S.K. Bhargava, B.M. Reddy, RSC Adv. 4 (2014) 43460–43469.
- [44] M.H. Amin, K. Mantri, J. Newnham, J. Tardio, S.K. Bhargava, Appl. Catal. B: Environ. 119–120 (2012) 217–226.
- [45] Z. Chen, F. Wang, H. Li, Q. Yang, L. Wang, X. Li, Ind. Eng. Chem. Res. 51 (2012) 202–212.
- [46] G. Park, L. Bartolome, K.G. Lee, S.J. Lee, D.H. Kim, T.J. Park, Nanoscale 4 (2012) 3879–3885.
- [47] M. Casapu, O. Kröcher, M. Mehning, M. Nachttegaal, C. Borca, M. Harfouche, D. Grolimund, J. Phys. Chem. C 114 (2010) 9791–9801.
- [48] J. Newnham, K. Mantri, M.H. Amin, J. Tardio, S.K. Bhargava, Int. J. Hydrogen Energy 37 (2012) 1454–1464.
- [49] S. Putla, M.H. Amin, B.M. Reddy, A. Nafady, K.A. Al Farhan, S.K. Bhargava, ACS Appl. Mater. Interfaces 7 (2015) 16525–16535.
- [50] B. Mallesham, P. Sudarsanam, B.V.S. Reddy, B.M. Reddy, Appl. Catal. B: Environ. 181 (2016) 47–57.
- [51] P. Sudarsanam, B. Mallesham, D.N. Durgasri, B.M. Reddy, J. Ind. Eng. Chem. 20 (2014) 3115–3121.
- [52] Y. Li, Z. Wei, F. Gao, L. Kovarik, R.A.L. Baylon, C.H.F. Peden, Y. Wang, ACS Catal. 5 (2015) 3006–3012.
- [53] P. Sudarsanam, B. Mallesham, P.S. Reddy, D. Großmann, W. Grünert, B.M. Reddy, Appl. Catal. B: Environ. 144 (2014) 900–908.
- [54] Y. Ren, J. Wang, X. Huang, B. Yang, J. Ding, RSC Adv. 5 (2015) 59208–59217.
- [55] C. Chen, G. Ding, D. Zhang, Z. Jiao, M. Wu, C.H. Shek, C.M.L. Wu, J.K.L. Lai, Z. Chen, Nanoscale 4 (2012) 2590–2596.
- [56] K. Subramani, D. Jayakumar, M. Sathish, Phys. Chem. Chem. Phys. 16 (2014) 4952–4961.
- [57] H. Rahaman, R.M. Laha, D.K. Maiti, S.K. Ghosh, RSC Adv. 5 (2015) 33923–33929.
- [58] P. Maitarad, J. Han, D. Zhang, L. Shi, S. Namuangruk, T. Rungrotmongkol, J. Phys. Chem. C 118 (2014) 9612–9620.
- [59] S. Zhang, X.-S. Li, B. Chen, X. Zhu, C. Shi, A.-M. Zhu, ACS Catal. 4 (2014) 3481–3489.
- [60] K.A. Michalow-Mauke, Y. Lu, K. Kowalski, T. Graule, M. Nachttegaal, O. Kröcher, D. Ferri, ACS Catal. 5 (2015) 5657–5672.
- [61] L. Zhang, L. Shi, L. Huang, J. Zhang, R. Gao, D. Zhang, ACS Catal. 4 (2014) 1753–1763.
- [62] X. Lu, C. Song, C.-C. Chang, Y. Teng, Z. Tong, X. Tang, Ind. Eng. Chem. Res. 53 (2014) 11601–11610.
- [63] A. Ramirez, P. Hillebrand, D. Stellmach, M.M. May, P. Bogdanoff, S. Fiechter, J. Phys. Chem. C 118 (2014) 14073–14081.
- [64] B. Mallesham, P. Sudarsanam, B.V.S. Reddy, B.M. Reddy, Appl. Catal. B: Environ. 181 (2016) 47–57.
- [65] M. Alhumaimess, Z. Lin, W. Weng, N. Dimitratos, N.F. Dummer, S.H. Taylor, J.K. Bartley, C.J. Kiely, G.J. Hutchings, ChemSusChem 5 (2012) 125–131.
- [66] J.W. Kim, K. Yamaguchi, N. Mizuno, Angew. Chem. Int. Ed. 47 (2008) 9249–9251.
- [67] X. Lang, H. Ji, C. Chen, W. Ma, J. Zhao, Angew. Chem. Int. Ed. 50 (2011) 3934–3937.
- [68] J. Beckers, G. Rothenberg, Green Chem. 12 (2010) 939–948.
- [69] C. He, B. Shen, J. Chen, J. Cai, Environ. Sci. Technol. 48 (2014) 7891–7898.